

Real-Time Tracking of Coherent Oscillations of Electrons in a Nanodevice by Photo-assisted Tunnelling

Yang Luo¹, Frank Neubrech^{1,2}, Alberto Martin-Jimenez¹, Na Liu^{1,2}, Klaus Kern^{1,3}, Manish Garg^{1,#}

¹ Max Planck Institute for Solid State Research, Heisenbergstr. 1, 70569 Stuttgart, Germany

² 2nd Physics Institute, University of Stuttgart, Pfaffenwaldring 57, 70569 Stuttgart, Germany

³ Institut de Physique, Ecole Polytechnique Fédérale de Lausanne, 1015 Lausanne, Switzerland

Author to whom correspondence should be addressed. mgarg@fkf.mpg.de

Coherent collective oscillations of electrons excited in metallic nanostructures (localized surface plasmons) can confine incident light to atomic scales and enable strong light-matter interactions, which depend nonlinearly on the local field. Direct sampling of such collective electron oscillations in real-time is crucial to performing petahertz scale optical modulation, control, and readout in a quantum nanodevice. Here, we demonstrate real-time tracking of collective electron oscillations in an Au bowtie nanoantenna, by recording photo-assisted tunnelling currents generated by such oscillations in this quantum nanodevice. The collective electron oscillations show a noninstantaneous response to the driving laser fields with a decay time of nearly 10 femtoseconds. The temporal evolution of nonlinear electron oscillations resulting from the coherent nonlinear optical response of the nanodevice were also traced in real-time. The contributions of linear and nonlinear electron oscillations in the generated tunnelling currents in the nanodevice were precisely determined. A coherent control of electron oscillations in the nanodevice is illustrated directly in the time domain. Functioning in ambient conditions, the excitation, coherent control, and read-out of coherent electron oscillations pave the way toward on-chip light-wave electronics in quantum nanodevices.

Interaction of light with metallic nanostructures can lead to a collective oscillation of conduction electrons. If the frequency of the incident light matches with the intrinsic resonance frequency of the collective electron oscillations (surface plasmons) in nanostructures, such oscillations can be dramatically amplified^{1,2}. The resulting strong electromagnetic field arising from the driven collective electron oscillations has now found many applications, ranging from atomic scale nano-optics³⁻⁶ to single molecule sensing⁷. Moreover, it enables exploring the nonlinear optical response of matter⁸⁻¹⁹. On interaction of strong electromagnetic fields with matter, nonlinearity in electron oscillations sets in, implying that the electron motion does not remain harmonic anymore. Anharmonic electronic motion implies that electrons oscillate with many frequencies, which are multiples of the driven frequency, in close analogy to a classical anharmonic (driven) oscillator.

In absence of the capability to directly resolve coherent electron oscillations in the time domain, interaction of light with matter has been studied by spectral measurements (in the UV to infrared range) utilizing the techniques of absorption spectroscopy and transient reflectivity^{20,21}. Signatures of nonlinearity in light-matter interactions in nanostructures have also been studied by spectral measurements, e.g. second and third harmonic generation²²⁻²⁴. Ultrafast techniques such as time-resolved two-photon photoemission^{25,26} (TR-2PPE) and time-resolved scanning near-field optical microscopy^{27,28} (TR-SNOM) have been successfully applied to monitor ultrafast plasmon dynamics at the nanoscale. Such measurements can retrieve the ultrafast evolution of the spatially dependent plasmonic electric fields^{29,30}, nevertheless, they do not capture the phase information of the frequency-dependent plasmon oscillations. A direct sampling of the ultrafast

coherent collective electron oscillations and the resulting local electric field in the time domain has not been reported yet, which is highly desired since it is the key to modern photonic functionalities operating at petahertz frequencies, ultrafast switching, and all-optical signal processing³¹⁻³⁵.

Here, we demonstrate a novel approach wherein both plasmon oscillations and nonlinear electron oscillations arising from the nonlinear optical response induced by ultrashort laser pulses in a strongly light-interacting quantum nanodevice can be traced directly in the time domain. Our nanodevice comprises of Au bowtie nanoantennas, with a junction gap of only a few nm. Electron oscillations in the nanodevice were traced by recording photo-assisted tunnelling currents. The plasmonic oscillations shows a noninstantaneous response to the driving electric field of the laser pulses with a decay time of ~ 10 fs. The spectral phase of the plasmonic field is highly dispersive in close agreement with a classical harmonic oscillator driven at its resonance frequency. Furthermore, we show that the contributions of linear and nonlinear electron oscillations in the generated photo-assisted tunnelling currents can be precisely deciphered and sampled in real time. Coherent control of plasmon oscillations directly in the time domain in the quantum nanodevice is also demonstrated.

Real-time sampling of coherent collective electron oscillations

In our experiments, arrays of seven identically designed Au bowtie nanoantennas (Fig. 1a) of ~ 300 nm size (isosceles triangle) with a junction gap of a few nm fabricated on top of a fused silica substrate (see section I in SM for details) were illuminated with two ultrashort laser pulses (pulse duration, $\tau_P \sim 7$ fs) of slightly different carrier frequencies. Fig. 1b shows a scanning electron microscope (SEM) image of seven Au bowtie nanoantennas. The plasmonic response of these nanoantennas as a function of incident laser wavelength and the spatial distribution of the local field enhancement in the junction were calculated by finite element simulations, as shown in Fig. 1c (see section II in SM for details). Owing to the high field enhancement at the junctions of the bowtie nanoantennas, plasmon oscillations will dominantly be excited when focusing the incident laser pulses in these nanoantenna junctions. In order to time resolve the plasmon oscillations induced by the ultrashort laser pulses, we probe the homodyne beating signal between plasmon oscillations induced by two ultrashort laser pulses with a very small difference in their carrier frequencies.

Here, we briefly explain the technique of homodyne beating, a self-referencing method to measure e.g. the phase of plasmon oscillations that are induced by the laser pulses in the nanoantennas (see section III in SM for details.). Ultrashort laser pulses ($\tau_P \sim 7$ fs) coming at a repetition rate of ~ 80 MHz (f_r) were passed through an acousto-optic-frequency-shifter (AOFS), which is driven at the frequency of $f_r + f_0$ as shown in Fig. 1d, f_0 is ~ 700 Hz. The 0th and 1st order diffraction beams coming from the AOFS are slightly shifted in their carrier frequencies, by f_0 . These two laser pulses are then combined and focused in the junction of

the nanoantennas, as schematically shown in Fig. 1e. The excited collective electron oscillations in the junction produce a local electric field, which can be expressed as a convolution of the incident laser field $E_i(t)$ and the optical response function ($R(t)$) of the nanoantennas; $E_{Li}(t) \propto E_i(t) * R(t)$, where the subscripts, $i = 1, 2$ denote the two different laser pulses. The net electric field produced by the electron oscillations induced by the two laser pulses at the junction of nanoantennas can then be expressed as;

$$E(t) = \sum_n \{E_{L1}(t) \exp(-inf_r t) + E_{L2}(t - \tau) \exp(-i(nf_r + f_0)(t - \tau)) + c.c.\} \quad (1)$$

where nf_r is the n^{th} (range from $\sim 3.5 \times 10^6$ to $\sim 6 \times 10^6$) multiple of the repetition rate of the laser pulses, τ represents the delay between the two pulses.

Due to the highly localized field enhancement in the nanoantenna junction, only the electrons close to the junction can be excited on interaction with photons and tunnel across the junction. A bias voltage is applied on the nanoantenna to facilitate the electron tunnelling processes. The mechanism of photo-assisted tunneling in the nanoantenna junction will be discussed later in the text. The single-photon assisted tunnelling of electrons induced e.g. by the plasmon oscillations in the nanoantenna junction is proportional to the linear polarization of the system; $I_1^T(t) \propto E(t)^2$, which contains terms oscillating at multiple frequencies. The very high-frequency terms, i.e. twice the carrier frequencies of the laser pulse, $2nf_r$ and $2nf_r + 2f_0$ ($\sim 0.6 \times 10^{15}$ Hz), cannot be lock-in detected (see section I in SM for details). Nevertheless, an interference term arising due to interference of the plasmon oscillations induced by the two laser pulses comes at the very small offset frequency of f_0 between the laser pulses; $I_1^T(t) \propto E_L(t)^2 \cos(f_0 t + nf_r \tau)$, assuming $E_L(t) = E_{L1}(t) = E_{L2}(t)$. This interference term contains both the amplitude and the phase information of the local electric field in the nanoantenna junction, which allows for a direct characterization of the plasmon oscillations.

A real-time sampling of the plasmon oscillations induced by the laser pulses with total pulse energy of ~ 100 pJ is shown in Fig. 2a. The plasmons undergo an oscillation period of ~ 2.6 fs. Fourier transform of the time trace in Fig. 2a reveals the spectral shape of the plasmonic response of the nanoantennas (Fig. 2b), which closely resembles the spectral shape of the plasmonic response evaluated from the finite element simulations (Fig. 1c and Fig. S2 in SM). A comparison of the spectrum of this plasmonic response with the spectrum of the incident laser pulses reveals significant spectral and temporal shaping of the laser pulses in the nanoantenna junction, as shown in Fig. 2b. A broad plasmonic response of the nanoantennas (Fig. 1c) implies a very fast damping rate of the induced plasmon oscillations, in the range of only a few fs³⁶. The

decay of the plasmon oscillations can be seen by a long and asymmetric oscillation trace on the positive side of the delay axis in Fig. 2a, as indicated by the black arrows.

Non-resonant excitation of bound electrons in a system is usually instantaneous, i.e. the electrons will oscillate in phase with the driving electric field and the oscillations will fade out as soon as the impetus from the driving field is over³⁷. However, when the electrons are excited on resonance, their response is with respect to the driving electric field and it has a much longer decay time. Such delayed response of bound electrons has been earlier reported for a dielectric medium^{37,38} as well as for an atom³⁹. Furthermore, another key distinctive feature of the resonant electron oscillations compared to the non-resonant case is their phase curve along the frequency axis. The phase curve around the resonance frequency is very dispersive, and the phase difference along the two extrema of the resonance frequency is $\sim \pi$ radians.

A bound electronic system, such as plasmons in the nanoantenna junction with the restoring force from the ions of the nanoantennas, can be simply modelled as a driven damped harmonic oscillator^{40,41}. The electric field of the plasmonic oscillations (E_{Pl}) can be expressed as;

$$E_{Pl}(t) \propto \int_{-\infty}^t \frac{1}{\omega_R} E_{Laser}(t') \exp(-\gamma(t-t')) \sin(\omega_R(t-t')) dt', \quad (2)$$

where ω_R is the resonance frequency of the plasmons, E_{Laser} is the electric field of the driving laser pulse, and γ is the intrinsic damping rate of the plasmon oscillations, which is determined by the bandwidth of the spectrum of the plasmonic resonance.

Fig. 2c shows a comparison of the calculated plasmonic field, considering a resonance frequency (ω_R) at ~ 1.6 eV and a damping rate γ of ~ 0.12 fs⁻¹, with the incident electric field of ~ 7 fs Fourier-limited laser pulse. The local electric field resulting from plasmon oscillations as measured in the experiment is in good agreement with the calculated plasmonic field as shown in Fig. 2c. A long tail associated with the damping of the plasmon oscillations along the positive delay axis can be clearly seen, which decays on the time scale of ~ 10 fs. A direct comparison of the experimentally measured plasmon oscillations, the electric field of the driving laser pulse, and the calculated plasmonic field is shown in Fig. S3 of the SM. The simulation also shows that the peak electric field of the plasmon oscillations is delayed by ~ 3 fs with respect to that of the driving laser pulse (Fig. 2c).

The spectrum and the phase of the plasmon oscillations as captured in the experiment are contrasted with those obtained from calculations (obtained by Fourier transform of E_{Pl}) in Fig. 2b. Plasmons undergo a spectral phase shift of nearly π radians across its resonance curve as also consistent with the model. The

spectrum of plasmon oscillations as simulated from the model is also in good agreement with the measurement. This consistency further attests the validity of the simple damped harmonic oscillator model describing the plasmon oscillations as measured in the experiments, and transparently demonstrates the capability of our technique to time resolve ultrafast plasmon oscillations. In addition to allowing access into the near-field plasmon oscillations (E_{pl}), an inversion of equation (2) also enables a direct measurement of the far field of the driving laser pulse.

Unravelling linear and nonlinear contributions in light-matter interaction

At higher field strength of the incident laser pulses, nonlinear electron oscillations, induced by higher order polarization responses of the nanoantenna junction set in due to the strong plasmon-enhanced light-matter interaction⁴² (see section III in SM). Fig. 3a shows the temporal evolution of the local second-order nonlinear oscillation of electrons induced at a total pulse energy of ~ 200 pJ. Photocurrent generated in the nanodevice due to the second-order nonlinear polarization response of the nanoantennas can also be measured with the homodyne beating technique; $I_2^T(t) \propto E(t)^2 E(t-\tau)^2 (1 - \cos(2f_0 t + 2nf_r \tau))$. A lock-in detection of the photocurrent signal at twice the offset frequency ($2f_0$) enables temporal sampling of the second-order nonlinear electron oscillations in the junction; entailing its complete phase information. At higher pulse energy, ~ 300 pJ, the third-order nonlinear oscillations of electrons, induced by three-photon absorption, can be recorded as shown in Fig. 3b; measured by performing lock-in detection at $3f_0$ frequency. However, the measurements at such high laser pulse energies is not very stable as the nanodevice is prone to physical damage. The oscillation periods of nonlinear electron oscillations for the case of 2nd and 3rd order optical responses are ~ 1.3 fs and ~ 0.9 fs, respectively. The spectral responses of 2nd and 3rd order nonlinear electron oscillations reveal a significant spectral shaping due to the multi-photon interactions in the nanoantenna junction, as shown in Fig. 3c and 3d.

In the weak-field or perturbative regime, light-matter interaction is usually characterized by a power-scaling experiment, wherein a physically relevant quantity is measured as a function of increasing intensity of the laser pulses. A n^{th} order nonlinearity implies the interaction with n number of photons to be dominated^{43,44}. Nevertheless, $n-1$ and $n-2$ photon orders in the light-matter interaction do not cease to exist, but their contributions are harder to access. A technique capable of deciphering the contribution of all photon-channels (linear and nonlinear polarizations) at a particular intensity of the laser pulse in the process of light-matter interaction is considerably sought after. Here, we demonstrate the technique of homodyne beating as a powerful tool to precisely decipher the contributions of different photon channels in the light-matter interaction.

The variation of the total photocurrent generated by the laser pulses in the junction of the nanoantennas as a function of the increasing intensity is shown in Fig. 3e (black data points), measured by intensity modulation (at ~ 520 Hz) of laser pulses. In a dual logarithmic plot, the scaling of the total photocurrent shows a switch from a linear scaling (slope of 1) at lower intensities to a quadrating scaling (slope of 2) at higher intensities of the laser pulses, indicating the contributions from both linear and nonlinear polarization responses of the nanoantenna junction at higher intensities. In order to disentangle the contributions of the different photon-channels, the variation of the photocurrent signal at zero delay between pulse-1 and pulse-2 (Fig. 1e, see also section I in SM) was measured as a function of intensity of the laser pulses for two different frequencies in the lock-in detection, f_0 and $2f_0$, as shown in Fig. 3e. The scaling of the lock-in signal at f_0 frequency is similar to the behaviour of the total photocurrent, since this signal can arise from both linear as well as local nonlinear polarization responses of the nanoantenna junction (with a prefactor of 0.5, see section III in SM for details). However, the signal at $2f_0$ frequency can only arise from the second-order nonlinear polarization response (with a prefactor of $1/8$). Thus, its scaling with respect to the intensity of the laser pulse is purely quadratic (Fig. 3e). This change from linear (dashed green curve) to quadratic (dashed orange curve) behaviour in the scaling of the total photocurrent signal in Fig. 3e occurs at the similar local field strength of the laser pulses where the signal at $2f_0$ frequency starts emerging, as indicated by a vertical black-dashed curve in Fig. 3e. Thus, demonstrating a direct measurement of the contribution of the 2nd order light-induced polarization response (nonlinear electron oscillations). We note that the pulse energies were kept below ~ 220 pJ in the measurement in Fig. 3e to avoid damage of the nanoantennas. The contribution of photocurrent at $3f_0$ frequency is too weak to be reproducibly determined, but in principle, can be measured with our technique. In conclusion, by recording the homodyne beating signal at f_0 and its harmonic frequencies ($2f_0$ and higher), we can precisely determine the contributions of linear and nonlinear electron oscillations (polarization responses) in the generated tunnelling currents in the nanodevice.

Photo-assisted electron tunnelling in the nanoantenna junction

In the following, we discuss the mechanism of photocurrent generation in the junction of the Au bowtie nanoantennas. The determination of the contributions of one- and two- photon processes in the power scaling measurements of the photocurrent signal in Fig. 3e excludes the mechanism of laser field-driven tunnelling in the nanoantenna junction, where a much less nonlinear power-dependent behaviour is expected. Besides, the Keldysh parameter for our pulses at the nanoantenna junction is above 4, where the laser field-driven tunnelling effects are virtually absent⁴⁴. In order to understand the mechanism underlying the photocurrent generation, we measured the variation of the photocurrent signal at f_0 frequency as a function of the increasing bias voltage applied in the nanoantenna junction, as shown in Fig. 4a. The photocurrent signal shows an extremely nonlinear dependence on the applied bias in the junction.

Therefore, over-the-barrier photoemission⁴⁴ can be excluded, as it would be virtually insensitive to the small biases applied in the junction. Moreover, the electrons excited by plasmon oscillations, following photoexcitation by laser pulses, can be up to approximately 1.5 eV above the Fermi level of Au, but, still significantly below the tunnelling barrier of Au (~ 5 eV) and cannot induce photoemission (photocurrent) in the measurement.

Here, we describe photocurrent generation by a simple model accounting for tunnelling of electrons across the nanoantenna junction with an effective Fermi electron distribution⁴⁵ that is photo-excited by the laser pulses, as shown schematically in Fig. 4b. In the case of photo-assisted tunnelling⁴⁶, electrons from one side of the junction are photo-excited via one-, two- or three-photon absorption and then tunnel to the other side through a reduced effective tunnelling barrier. The calculated electron tunnelling probability as a function of increasing bias (see section V in SM) for a junction of gap-width of ~ 1.2 nm matches quite well with the experimentally measured nonlinearity of the photocurrent signal (Fig. 4a). The junction (tunnel) gap of ~ 1.2 nm is significantly bigger for any DC tunnelling (below 5 V) but not for photo-assisted tunnelling. It is worth mentioning that the designed junction gap of the nanoantennas is ~ 10 nm. However, at such small dimensions one reaches the limitation of the state-of-the-art lithographic techniques. The actual junction gap can be significantly smaller due to spillage of Au during the fabrication process and electromigration of Au atoms in the nanoantenna junction by the applied DC bias in the device⁴⁷.

Real-time coherent control of localized plasmon oscillations

We illustrate that the collective electron oscillations induced by the laser pulses can be coherently controlled by varying the CEP of the laser pulses, directly in the time domain. A modulation of the CEP of the laser pulse controls the CEP of the laser-induced polarization, which in turn coherently modulates the CEP of the driven plasmon oscillations. As the technique presented in this work is a self-referencing technique, we probe linear plasmon oscillations induced in the junction of the nanoantennas by varying the CEP of one of the laser pulses (pulse-1 in Fig. 1d), while keeping the CEP of the other pulse fixed (pulse-2 in Fig. 1d). The CEP of the 1st order diffracted pulse (pulse-1) is controlled by varying the phase of the radio frequency phase-shifter (see section III in SM) driving the AOFs. Fig. 5a shows the temporal evolutions of plasmon (electron) oscillations as a function of the varying CEP of pulse-1. Four representative traces at the CEP of $0, 0.5\pi, \pi,$ and 1.5π are shown in Fig. 5b. Coherent control of plasmon (electron) oscillations as evident by a linear movement of the maxima of the oscillations on change of the CEP can be clearly seen in Fig. 5a and Fig. 5b.

Conclusion

Direct measurement of light-waves can enable the study of quantum properties of ultrashort pulses, e.g. quantum fluctuations associated with the ground state of the electric field and squeezing of light. By utilizing the technique of optical homodyne beating, the electronic polarization response of a single molecule trapped in the junction of the nanodevice can be traced in the time-domain⁴⁸; this polarization response will have the fingerprints of molecular electronic and vibrational levels. The capability to coherently trigger, measure and control collective electron oscillations and the associated coherent multi-photon processes open new prospects for understanding strong light-matter interaction in solids directly in the time domain as well as pave the way towards on-chip light-wave electronics at petahertz switching and read-out frequency^{49,50}.

Contributions

M.G. conceived the project and designed the experiments. K.K. supervised the project. Y.L., M.G., A.M.J built the experimental set-up, performed the experiments and analyzed the experimental data. F.N. and N.L. contemplated the design of the nanodevices and fabricated the nanodevices. F.N. performed the finite element analysis simulations. All authors interpreted the results and contributed to the preparation of the manuscript.

Acknowledgments

We thank Javier Aizpurua, Andrey Borissov and Shaoxiang Sheng for fruitful discussions and Wolfgang Stiepany and Marko Memmler for technical support. A.M.J acknowledges the Alexander von Humboldt Foundation for financial support.

References

- 1 Maier, S. A. *et al.* Plasmonics - A route to nanoscale optical devices. *Adv. Mater.* **13**, 1501-1505 (2001).
- 2 Jiang, N. N., Zhuo, X. L. & Wang, J. F. Active Plasmonics: Principles, Structures, and Applications. *Chem. Rev.* **118**, 3054-3099 (2018).
- 3 Barbry, M. *et al.* Atomistic Near-Field Nanoplasmonics: Reaching Atomic-Scale Resolution in Nanooptics. *Nano Lett.* **15**, 3410-3419 (2015).

- 4 Schotz, J. *et al.* Onset of charge interaction in strong-field photoemission from nanometric needle tips. *Nanophotonics-Berlin* **10**, 3769-3775 (2021).
- 5 Forg, B. *et al.* Attosecond nanoscale near-field sampling. *Nat. Commun.* **7** (2016).
- 6 Dombi, P. *et al.* Strong-field nano-optics. *Rev. Mod. Phys.* **92** (2020).
- 7 Zhang, R. *et al.* Chemical mapping of a single molecule by plasmon-enhanced Raman scattering. *Nature* **498**, 82-86 (2013).
- 8 Bionta, M. R. *et al.* On-chip sampling of optical fields with attosecond resolution (Apr, 10.1038/s41566-021-00792-0, 2021). *Nat. Photon.* **15**, 787-787 (2021).
- 9 Rybka, T. *et al.* Sub-cycle optical phase control of nanotunnelling in the single-electron regime. *Nat. Photon.* **10**, 667-670 (2016).
- 10 Putnam, W. P., Hobbs, R. G., Keathley, P. D., Berggren, K. K. & Kartner, F. X. Optical-field-controlled photoemission from plasmonic nanoparticles. *Nat. Phys.* **13**, 335-339 (2017).
- 11 Blochl, J. *et al.* Spatiotemporal sampling of near-petahertz vortex fields. *Optica* **9**, 755-761 (2022).
- 12 Herink, G., Solli, D. R., Gulde, M. & Ropers, C. Field-driven photoemission from nanostructures quenches the quiver motion. *Nature* **483**, 190-193 (2012).
- 13 Kruger, M., Schenk, M. & Hommelhoff, P. Attosecond control of electrons emitted from a nanoscale metal tip. *Nature* **475**, 78-81 (2011).
- 14 Piglosiewicz, B. Carrier-envelope phase effects on the strong-field photoemission of electrons from metallic nanostructures. *Nat. Photon.* **8**, 79-79 (2014).
- 15 Dombi, P. *et al.* Strong-field nano-optics. *Rev. Mod. Phys.* **92**, 025003 (2020).
- 16 Ludwig, M. *et al.* Sub-femtosecond electron transport in a nanoscale gap. *Nat. Phys.* **16**, 341-345 (2020).
- 17 Liu, Y. Y., Beetar, J. E., Nesper, J., Gholam-Mirzaei, S. & Chini, M. Single-shot measurement of few-cycle optical waveforms on a chip. *Nat. Photon.* **16**, 109-112 (2022).
- 18 Fischer, M. P. *et al.* Field-resolved detection of the temporal response of a single plasmonic antenna in the mid-infrared. *Optica* **8**, 898-903 (2021).
- 19 Heide, C. *et al.* Electronic Coherence and Coherent Dephasing in the Optical Control of Electrons in Graphene. *Nano Lett.* **21**, 9403-9409 (2021).
- 20 Kravets, V. G., Kabashin, A. V., Barnes, W. L. & Grigorenko, A. N. Plasmonic Surface Lattice Resonances: A Review of Properties and Applications. *Chem. Rev.* **118**, 5912-5951 (2018).
- 21 Lin, Y. B., Zou, Y. & Lindquist, R. G. A reflection-based localized surface plasmon resonance fiber-optic probe for biochemical sensing. *Biomed. Opt. Express* **2**, 478-484 (2011).
- 22 Kauranen, M. & Zayats, A. V. Nonlinear plasmonics. *Nat. Photon.* **6**, 737-748 (2012).

- 23 Panoiu, N. C., Sha, W. E. I., Lei, D. Y. & Li, G. C. Nonlinear optics in plasmonic nanostructures. *J. Optics UK* **20** (2018).
- 24 Butet, J., Brevet, P. F. & Martin, O. J. F. Optical Second Harmonic Generation in Plasmonic Nanostructures: From Fundamental Principles to Advanced Applications. *ACS Nano* **9**, 10545-10562 (2015).
- 25 Dabrowski, M., Dai, Y. N. & Petek, H. Ultrafast Photoemission Electron Microscopy: Imaging Plasmons in Space and Time. *Chem. Rev.* **120**, 6247-6287 (2020).
- 26 Davis, T. J. *et al.* Ultrafast vector imaging of plasmonic skyrmion dynamics with deep subwavelength resolution. *Science* **368**, 386 (2020).
- 27 Huber, M. A. *et al.* Femtosecond photo-switching of interface polaritons in black phosphorus heterostructures. *Nat. Nanotechnol.* **12**, 207-211 (2017).
- 28 Wagner, M. *et al.* Ultrafast Dynamics of Surface Plasmons in InAs by Time-Resolved Infrared Nanospectroscopy. *Nano Lett.* **14**, 4529-4534 (2014).
- 29 Dai, Y. A. *et al.* Plasmonic topological quasiparticle on the nanometre and femtosecond scales. *Nature* **588**, 616 (2020).
- 30 Dreher, P., Janoschka, D., Frank, B., Giessen, H. & Heringdorf, F. J. M. Z. Focused surface plasmon polaritons coherently couple to electronic states in above-threshold electron emission. *Commun Phys-Uk* **6** (2023).
- 31 Boolakee, T. *et al.* Light-field control of real and virtual charge carriers. *Nature* **605**, 251-255 (2022).
- 32 Garg, M. *et al.* Multi-petahertz electronic metrology. *Nature* **538**, 359-363 (2016).
- 33 Steinmeyer, G. A review of ultrafast optics and optoelectronics. *J. Opt. A. Pure Appl. Op.* **5**, R1-R15 (2003).
- 34 Sommer, A. *et al.* Attosecond nonlinear polarization and light-matter energy transfer in solids. *Nature* **534**, 86-90 (2016).
- 35 Sederberg, S. *et al.* Attosecond optoelectronic field measurement in solids. *Nat. Commun.* **11**, 1-8 (2020).
- 36 Csete, M., Szenes, A., Vass, D., Banhelyi, B. & Dombi, P. Few-cycle localized plasmon oscillations. *Sci. Rep.* **10**, 1-10 (2020).
- 37 Hofmann, M. *et al.* Noninstantaneous polarization dynamics in dielectric media. *Optica* **2**, 151-157 (2015).
- 38 Hui, D. *et al.* Attosecond electron motion control in dielectric. *Nat. Photon.* **16**, 33 (2022).
- 39 Hassan, M. T. *et al.* Optical attosecond pulses and tracking the nonlinear response of bound electrons. *Nature* **530**, 66-70 (2016).

- 40 Zuloaga, J. & Nordlander, P. On the Energy Shift between Near-Field and Far-Field Peak Intensities in Localized Plasmon Systems. *Nano Lett.* **11**, 1280-1283 (2011).
- 41 Song, H. B., Lang, P., Ji, B. Y., Song, X. W. & Lin, J. Q. Controlling the dynamics of the plasmonic field in the nano-femtosecond scale by chirped femtosecond laser pulse. *Opt. Mater Express* **11**, 2817-2827 (2021).
- 42 Reutz, M., Li, A. D. & Petek, H. Coherent Two-Dimensional Multiphoton Photoelectron Spectroscopy of Metal Surfaces. *Phys Rev X* **9** (2019).
- 43 Schafer, K. J. & Kulander, K. C. High harmonic generation from ultrafast pump lasers. *Phys. Rev. Lett.* **78**, 638-641 (1997).
- 44 Krausz, F. & Ivanov, M. Attosecond physics. *Rev. Mod. Phys.* **81**, 163-234 (2009).
- 45 Simmons, J. G. Generalized formula for the electric tunnel effect between similar electrodes separated by a thin insulating film. *J. Appl. Phys.* **34**, 1793-1803 (1963).
- 46 Schroder, B. *et al.* Controlling photocurrent channels in scanning tunneling microscopy. *New J. Phys.* **22**, 033047 (2020).
- 47 Yang, Y. J. *et al.* Light phase detection with on-chip petahertz electronic networks. *Nat. Commun.* **11** (2020).
- 48 Garg, M. *et al.* Real-space subfemtosecond imaging of quantum electronic coherences in molecules. *Nat. Photon.* **16**, 196-202 (2022).
- 49 Hui, D. *et al.* Ultrafast optical switching and data encoding on synthesized light fields. *Science Advances* **9**, 1-7 (2023).
- 50 Boolakee, T. *et al.* Light-field control of real and virtual charge carriers. *Nature* **605**, 251 (2022).

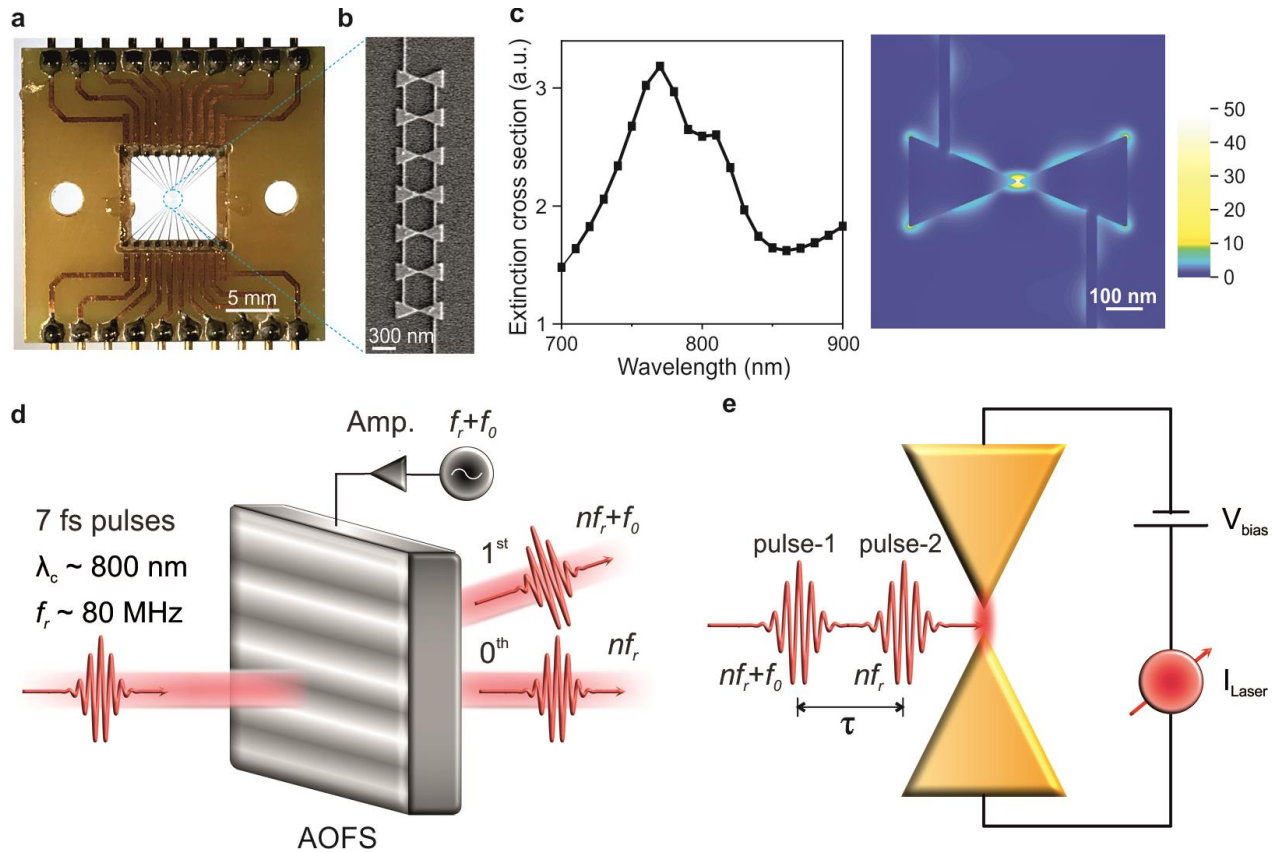


Figure 1 | **a**, Nanodevice and optical homodyne beating technique for tracing coherent oscillations of electrons. **a**, Photograph of the nanodevice. The nanodevice consists of a series of seven connected, identically designed, Au bowtie nanoantennas fabricated on top of a fused silica substrate. **b**, A scanning electron microscope (SEM) image of seven bowties. **c**, Numerically calculated plasmonic response (left panel) of a single Au bowtie (junction size of 10 nm) showing the 2nd order resonance as deduced from the spatial near field distribution (right panel) at 770 nm. The local field-enhancement factor (E/E_0) is denoted by the colour code in the colour bar. In the simulations, the electrical field is polarized along the long bowtie axis. **d**, Laser pulses with a very small offset frequency, f_0 , in their carrier frequencies are generated by selecting the zeroth-order beam $E_1(nf_r)$ ‘pulse-1’ and first-order diffracted beam $E_2(nf_r+f_0)$ ‘pulse-2’ of laser pulses traversing through an acousto-optic frequency shifter (AOFS). **e**, Schematic illustration of the optical homodyne beating technique: zeroth and first order diffracted laser pulses from the AOFS are combined and focused onto the nanodevice. Photocurrent generated by the laser pulses in the nanodevice is measured by lock-in detection at the offset frequency of f_0 .

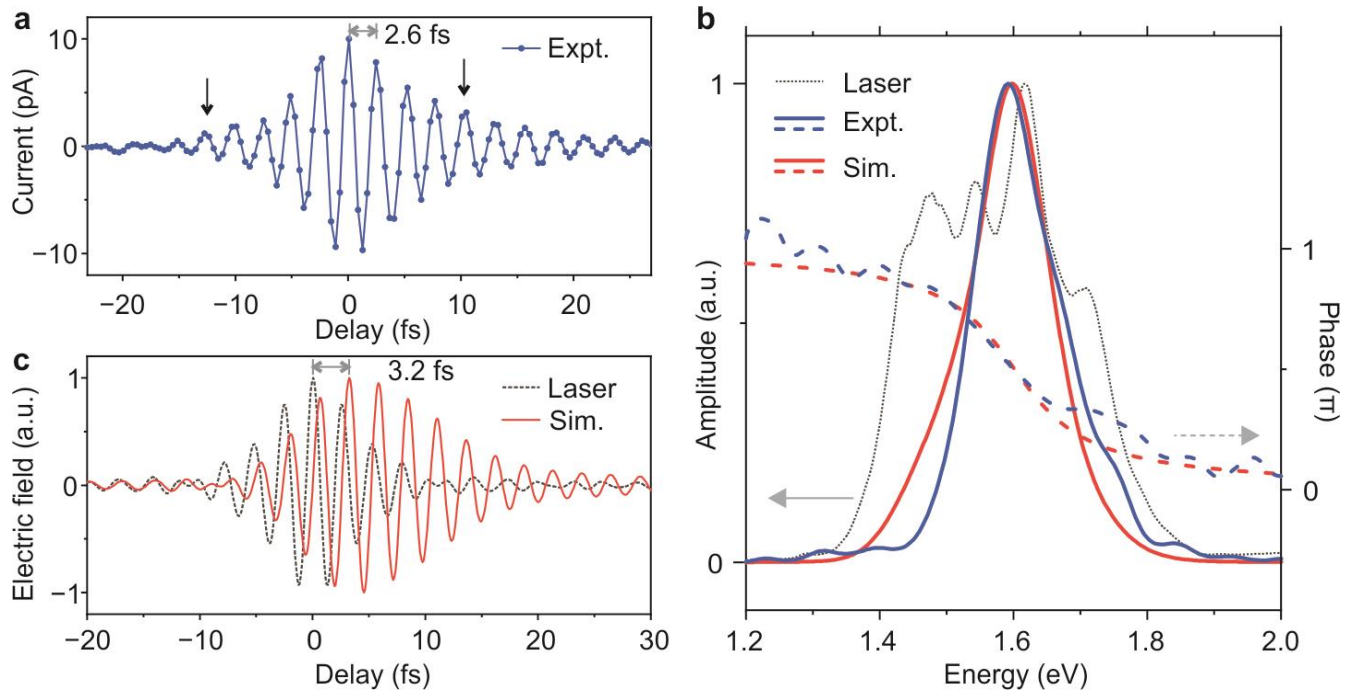


Figure 2| Real-time tracking of coherent collective electron oscillations. **a**, Variation of the laser-induced photocurrent as a function of the delay between pulse-1 and pulse-2 laser pulses of slightly different carrier frequencies (Fig. 1e) in a biased nanodevice, with the bias in the nanoantenna junction being 2.5 V. **b**, Comparison of the experimental and calculated plasmonic response in the nanoantenna junction. The dashed-blue and dashed-red curves represent the phases of experimentally measured and theoretically simulated plasmonic oscillations, respectively. The dotted-black curve shows the spectrum of the incident laser pulses on the nanoantenna junction. **c**, Comparison of the electric field of ~ 7 fs long driving laser pulse (dashed black curve) with the theoretically calculated plasmonic field (solid blue curve). Black double arrow indicates a delayed response of the plasmonic oscillations with respect to the electric field of the driving laser pulse.

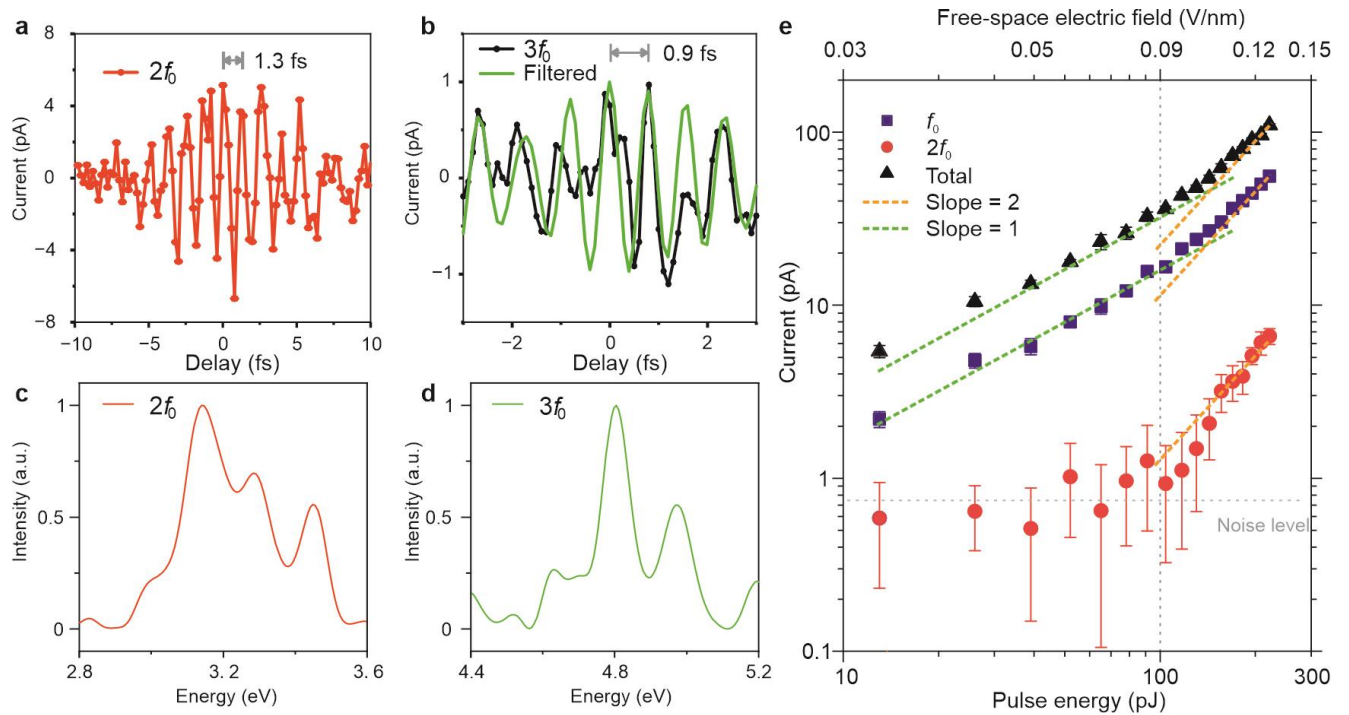


Figure 3 | Quantifying single and multi-photon light-matter interactions. **a, b** Variation of the laser-induced photocurrent as a function of the delay between pulse-1 and pulse-2 laser pulses measured at the lock-in frequency of $2f_0$ and $3f_0$, respectively. The bias in the nanoantenna junction is 3.0 V. **c**, Spectral response of the time-resolved electron oscillations in **a** (red-curve). **d**, Spectral response of the time-resolved electron oscillations in **b** (green-curve). **e**, Measured variation of the photo-assisted tunnelling current as a function of increasing field-strength of the incident laser pulses (top x-axis) on the nanodevices. Violet and red-points show the variation of the photocurrent signal measured with the lock-in detection frequency of f_0 and $2f_0$, respectively. Measurements were performed at the zero-delay between pulse-1 and pulse-2 (Fig. 1e). Peak-field strength refers to the maximum of the net electric field produced by the two pulses. Black-points show the variation of the total photo-assisted tunnelling current generated in the nanodevice. Dashed green and orange curves indicate a slope of one (linear) and two (quadratic) in the dual logarithmic plot.

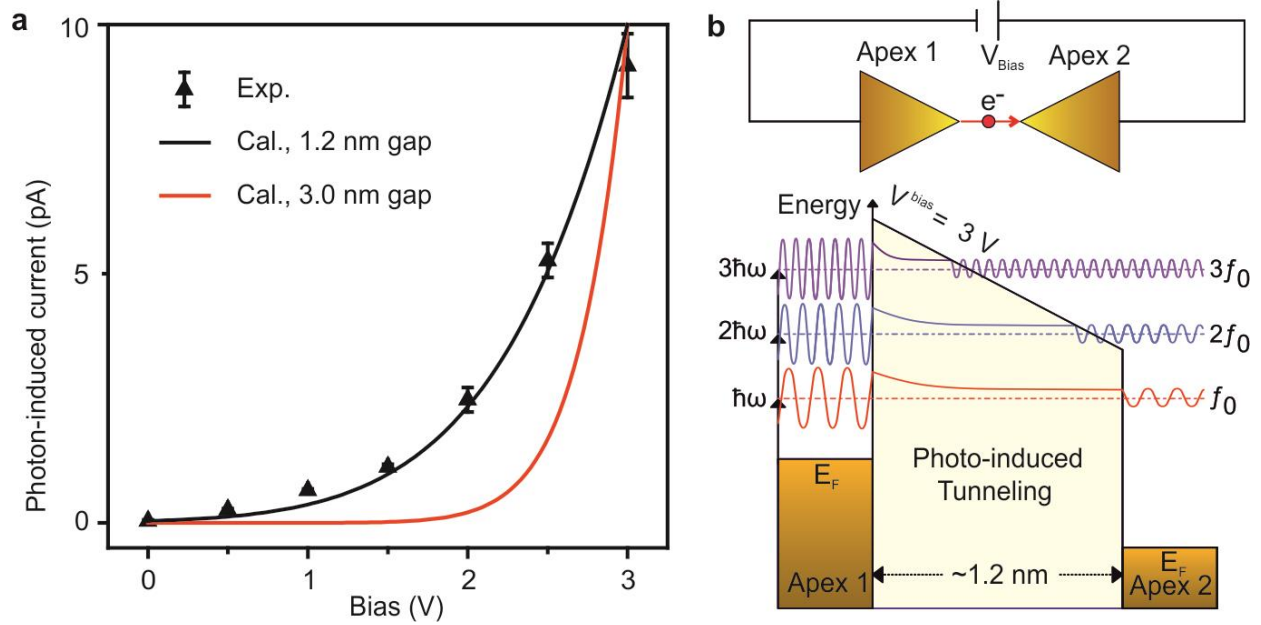


Figure 4| Photo-assisted electron tunnelling in the nanoantenna junction. a, Black points: Variation of the photocurrent signal measured at the lock-in frequency of f_0 as a function of the increasing bias in the nanodevice. The pulse energy of the laser pulses was set at ~ 100 pJ and the delay between the pulses (pulse-1 and pulse-2) was set to zero. Black and red-curves show the calculated electron tunnelling probability, considering only single-photon excitation as a function of the increasing bias in the nanoantenna junction, where the junction gap is 1.2 and 3 nm, respectively. **b**, Bottom-panel: Schematic of the energy-level alignment in the biased nanodevice. Fermi level (E_F) of the Au nanoantenna on the left side (Apex 1, top-panel) is upshifted with respect to the Fermi level of the nanoantenna on the right side (Apex 2, top-panel). Electron oscillations above the Fermi level stimulated by one-, two- or three-photon absorption, can lead to photo-assisted electron tunnelling to the other side of the junction, as also schematically illustrated in the top-panel.

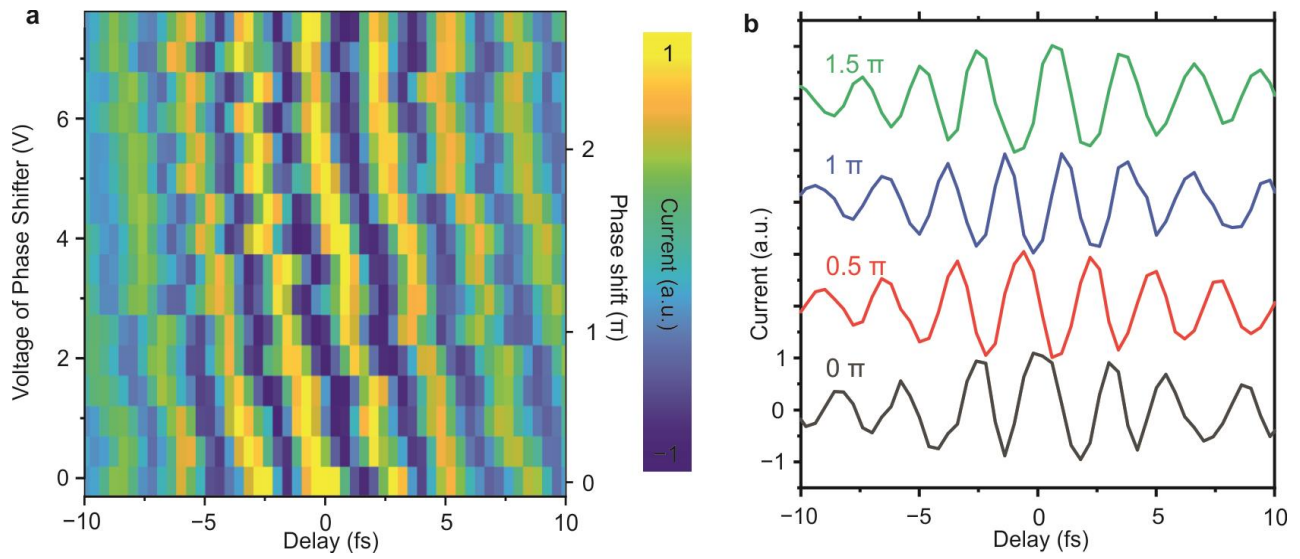


Figure 5| Coherent control of plasmon oscillations. **a**, A series of time-resolved plasmonic oscillations measured as a function of the CEP of pulse-1 in the nanodevice. The CEP of pulse-2 was kept fixed. Electron oscillations were sampled at the lock-in frequency of f_0 . **b**, Measured temporal variation of electron oscillations from the measurement in **a** for four different CEPs of pulse-1. The CEPs of the pulse-1 are annotated on top of each curve. The traces are shifted vertically for clarity.

Supplementary Materials for

Real-Time Tracking of Coherent Oscillations of Electrons in a Nanodevice by Photo-assisted Tunnelling

Yang Luo¹, Frank Neubrech^{1,2}, Alberto Martin-Jimenez¹, Na Liu^{1,2}, Klaus Kern^{1,3}, Manish Garg^{1,#}

¹ Max Planck Institute for Solid State Research, Heisenbergstr. 1, 70569 Stuttgart, Germany

² 2nd Physics Institute, University of Stuttgart, Pfaffenwaldring 57, 70569 Stuttgart, Germany

³ Institut de Physique, Ecole Polytechnique Fédérale de Lausanne, 1015 Lausanne, Switzerland

[#] Author to whom correspondence should be addressed. mgarg@fkf.mpg.de

Section I. Experimental Details

1.1. Nanodevice Fabrication

The devices were fabricated on fused silica substrates using electron beam lithography, evaporation, and lift-off techniques. One device consists of ten arrays, each containing seven bowties with identically designed geometric dimensions and junctions, (see Fig. 1 in the main-text). In the design, the opposing isosceles triangles (triangle height of 300 nm, base of 250 nm) forming the bowtie are separated by gap sizes of 10 nm, 5 nm, 0 nm, and -5nm. The designed sizes of the junctions, e.g. 5 nm, are identical for all bowties in one array. Negative gap sizes indicate merged (overlapping) triangles. Please note that the fabricated gap sizes will differ from the designed values due to the proximity effect and exposure characteristics of the resist. The electrical connections are fanned out allowing to electrically connect and address every bowtie array individually. In addition, two bowtie arrays are replaced by a rectangle of 1 x 3.5 microns (short cut scenario) allowing for electrical reference measurements.

For nanofabrication, 80 nm or CSAR 62 resist (Allresist) was spin-coated on a fused silica substrate (10 mm x 10 mm) and baked for 60 s at 180° C. To avoid charging during electron exposure with the Raith Eline Plus system, a layer of ESPACER 300Z (Showa Denko, Singapore) was spin-coated (5000 rpm for 60 s) on top of the CSAR 62 resist. The patterning of the nanostructures (bowties and 30 nm narrow electrical connections, see electron micrograph in figure 1) was performed with an electron beam energy of 20 keV, a current of 0.02 nA and a dose of 130 $\mu\text{C}/\text{cm}^2$. To fabricate nanometer-sized gaps, corrections for the proximity effect were included in the design process and the movement of the electron beam was optimized. The micro- and millimeter-sized structures (contact pads and electronic connections, see image in Fig. 1, main-text) were patterned in the same exposure step with the same energy and dose, but a larger electron current (9.5 nA). After exposure, the conducting ESPACER was removed in ultrapure water (2 s). Subsequently, the resist was developed in AR 600-546 (Allresist) for 60 s, stopped in AR 600-60 (Allresist) for 30 s and immersed in propan-2-ol for 30 s. Using electron beam evaporation at a pressure of 5×10^{-7} mbar, a chromium (Cr) adhesion layer of 3 nm followed by 30 nm of gold (Au) has been deposited on the developed sample. Lift-off in N-Ethyl-2-pyrrolidon (Allresist) at 80°C was performed for at

least 8 hours, to remove the gold-covered and non-exposed CSAR resist and reveal the fabricated structure.

1.2 Experimental Set-up

In our experiments, CEP-stable ultrashort laser pulses were split into two arms of the Mach-Zehnder interferometer (Fig. S1) by a beam splitter (BS). Laser pulses in one arm of the interferometer were loosely focused onto an acousto-optic-frequency-shifter (AOFS) by a bi-convex lens of a focal length of ~ 25 cm. A transverse radio frequency wave of frequency $f_r + f_0$ (~ 80 MHz + 700 Hz) runs through the AOFS with the average power of the incident laser pulses being ~ 300 mW. The fused silica AOFS is driven by an arbitrary waveform synthesizer and the power of the radio frequency (RF) wave is amplified by an RF amplifier up to ~ 2 W as schematically shown in Fig. S1. The 0th order diffracted beam out of the AOFS is blocked, whereas the 1st order frequency upshifted laser beam (see also section II) is combined with the laser pulses from the other arm of the interferometer. The two combined laser pulses (pulse-1 and pulse-2 in Fig. 1e, main-text) are then focused by an off-axis parabolic mirror (OAPM) of focal length ~ 2.5 cm to the bowtie nanoantenna device mounted on a precision 3D stage. Markers in the nanodevice and a high zoom objective ($10\times$) placed behind the nanodevice enable the precise positioning of the nanoantenna junction in the laser focal spot (~ 10 μm diameter). The photo-assisted tunneling current induced by the ultrashort laser pulses in the nanoantenna junction is amplified by a high gain ($\times 10^9$ V/A) current amplifier (Femto, DLPCA-200) and measured with a lock-in amplifier.

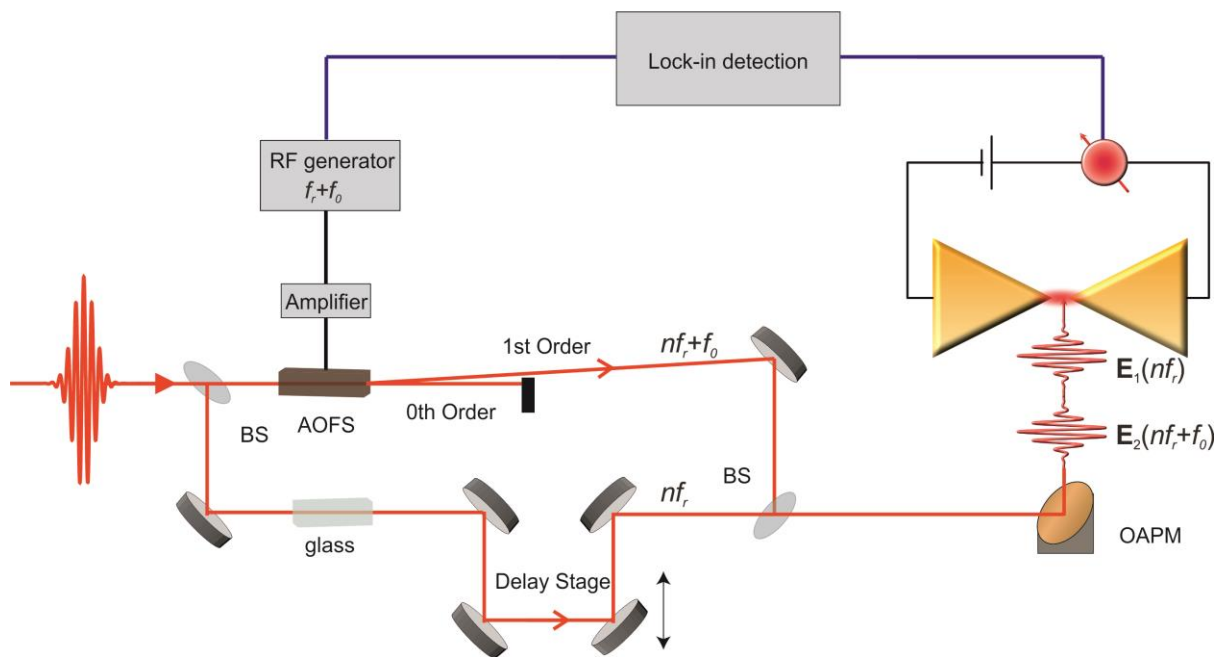


Fig. S1 | Schematic of the experimental set-up. BS: Beam splitter. AOFS: Acousto Optic Frequency Shifter. RF generator: Radio frequency signal generator. OAPM: Off-Axis Parabolic Mirror.

Section II. Finite element simulations of a single bowtie

Numerical simulations were performed using the commercial software COMSOL Multiphysics based on a finite element method. A single bowtie structure is implemented by two identically but opposing isosceles triangles with a base of 250 nm and a height of 300 nm supported by a substrate. The opposing tips and edges of the bowties are modelled with fillets (radius of 5 nm). The height of the bowtie is 30 nm and a junction size of 10 nm is exemplarily selected. The dielectric function of gold was taken from Johnson and Christy¹ and the refractive index of the fused silica substrate was approximated with 1.5 in the spectral range of interest. A refined mesh size of at least 1 nm was used in a volume (50 nm x 50 nm x 50 nm) centered in the bowtie junction to map the fine features of the junction. Perfectly matched layers were placed around the simulation domain to completely absorb the waves leaving the domain. The spectral response and the 2D electrical field distributions of a single bowtie structure are numerically calculated using full field formulation and background field conditions.

Figure S2 shows the extinction cross section of a single bowtie with the abovementioned

dimensions. The insets depict the electrical field distributions (taken at the half height of the bowtie) normalized to the background electrical field at the respective wavelengths. The polarization of the incident electrical field is parallel to the bowtie axis. Based on the field distributions we identify the peak at 1420 nm as the first order plasmonic mode and the peaks at 770 nm and 810 nm as a higher order excitation originating from the hybridization of the two opposing isosceles triangles. The double peak feature results from plasmonic excitations in the electrical connections and is not present for bowties without electrical connections (not shown). The shoulder at ~ 1150 nm has the same origin.

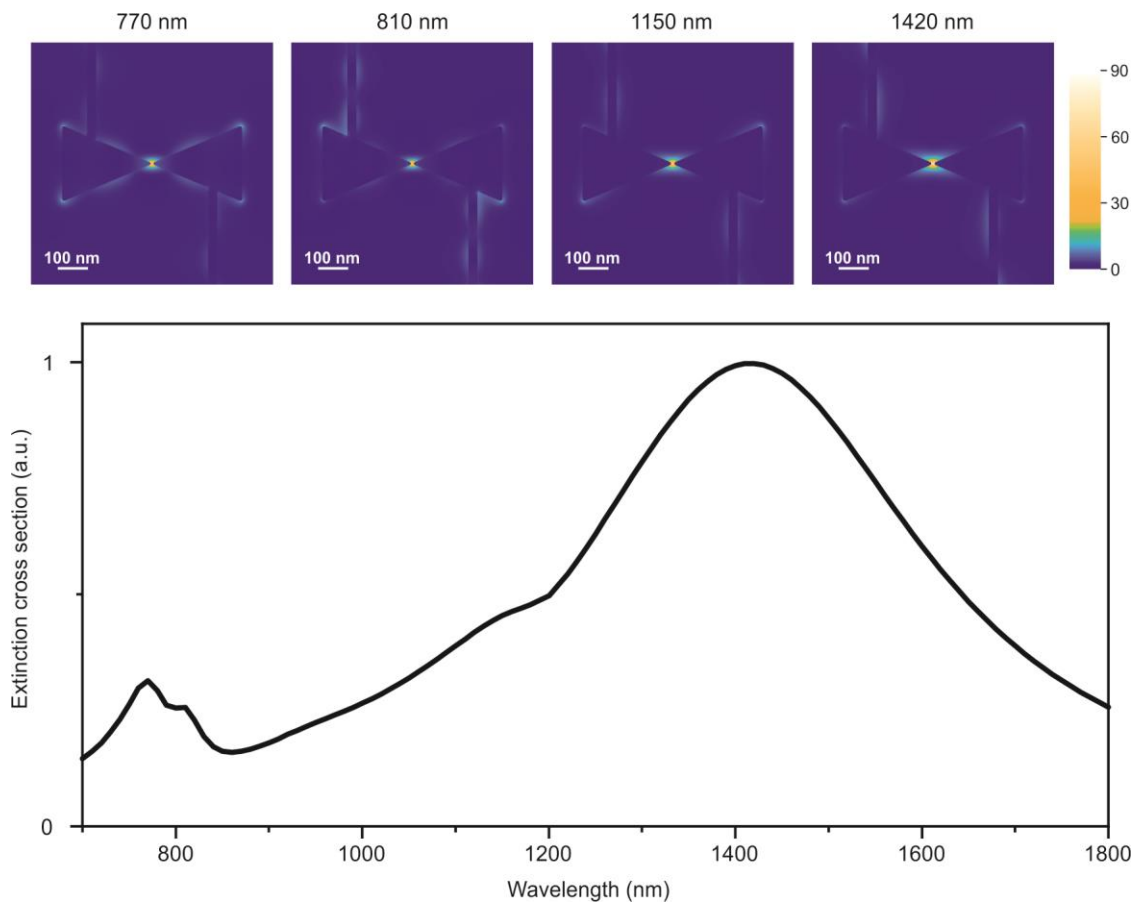


Fig. S2 | Bottom Panel: Simulated extinction cross section of a single bowtie as a function of the wavelength with dimensions given in the text. Top Panels: Distributions of the enhanced near fields at different wavelengths.

Section III. Homodyne beating detection of the photo-assisted tunnelling current in Nanodevices

An ultrashort CEP stable laser pulse produced in a mode-locked oscillator entails an underlying frequency comb, whose teeth are separated by the repetition rate ($f_r \sim 80$ MHz) of the oscillator. The frequency comb spans over the entire spectral bandwidth of the laser pulses, i.e. from 650 nm to 1050 nm, with the central wavelength of the spectrum being at ~ 810 nm. The electric field of this laser pulse in the frequency domain can be expressed as

$$E_1(f_1) = \sum_n \varepsilon(f_n) \delta(f - f_n) e^{ik \cdot r}, \quad (1)$$

where $f_n = nf_r$, is the n^{th} multiple of the repetition rate of the laser pulses. $\delta(f - f_n)$ is the Dirac delta function describing the position of an individual tooth of the frequency comb, which are separated from each other by f_r and $\varepsilon(f_n)$ describes the spectral weight of each individual comb line in the laser spectrum. The central (or the carrier) frequency (f_1) of our laser pulses is $\sim 0.37 \times 10^{15}$ Hz (for a central wavelength of $\lambda \sim 810$ nm), implying that $n \sim \frac{f_1}{f_r}$ is approximately 4.6×10^6 . This frequency comb is emitted in every shot from the oscillator at its repetition rate.

On interaction with the radio frequency (RF) wave in the acousto-optic-frequency-shifter (AOFS) being driven at the frequency of $f_r + f_0$, the ultrashort laser pulses undergo diffraction (Fig. 1d, main-text). The frequency comb of the 1st order diffracted laser pulse ('pulse-1' in Fig. 1e) out of the AOFS is upshifted in the frequency by $f_r + f_0$ with respect to the zeroth order laser pulse ('pulse-2' in Fig. 1e). The electric field of the first-order diffracted laser pulse from the AOFS can be expressed as;

$$\begin{aligned} E_2(f_2) &= \sum_n \varepsilon(f_n + f_r + f_0) \delta(f - f_n - f_r - f_0) e^{ik \cdot r} \\ E_2(f_2) &= \sum_n \varepsilon((n+1)f_r + f_0) \delta(f - (n+1)f_r - f_0) e^{ik \cdot r} \end{aligned} \quad (2)$$

Since the order of the frequency comb lines n is much greater than 1 ($n \sim 4.6 \times 10^6$), implying $(n+1) \sim n$, the above equation simplifies to

$$E_2(f_2) = \sum_n \varepsilon(nf_r + f_0) \delta(f - nf_r - f_0) e^{ik \cdot r}$$

$$E_2(f_2) = \sum_n \varepsilon(f_n + f_0) \delta(f - f_n - f_0) e^{ik \cdot r} \quad (3)$$

Thus, the offset between the carrier frequencies of the 1st and 0th order diffracted laser pulses is only $\sim f_0$. The excited collective electron oscillations in the junction will produce a local electric field, which can be expressed as a convolution of the incident laser field $E_i(t)$ and the optical response function ($R(t)$) of the nanoantennas; $E_{L_i}(t) \propto E_i(t) * R(t)$, where the subscripts, $i = 1, 2$ denote the two different laser pulses (pulse-1 and pulse-2, in Fig. 1e). The net electric field generated by the combination of the two pulses (0th and 1st order diffracted beams, E_1 and E_2) with a delay τ between them at the nanoantenna junction, in the time domain can be written as:

$$E(t) = E_{L_1}(t) \exp(-if_1 t) + E_{L_2}(t - \tau) \exp(-i(f_1 + f_0)(t - \tau)) + c.c \quad (4)$$

where f_1 is the carrier frequency of the 0th order diffracted beam (pulse-2 in Fig. 1e). The total polarization response (linear as well as nonlinear) induced in the nanoantenna junction owing to its interaction with the ultrashort pulses can be expressed as;

$$P(t) \propto \chi^{(1)} E(t) + \chi^{(2)} E(t)^2 + \chi^{(3)} E(t)^3 + \dots \quad (5)$$

where $\chi^{(1)}$, $\chi^{(2)}$ and $\chi^{(3)}$ are linear, second and third order optical susceptibilities, respectively.

Photo-assisted tunnelling current (I_1^T) generated in the nanoantenna junction due to the linear polarization response (one-photon absorption) of the nanoantennas will be proportional to the square of the net first order polarization response induced by the two laser pulses.

$$I_1^T(t) \propto \chi_1^2 E(t)^2$$

$$I_1^T(t) \propto \chi_1^2 \left\{ E_{L_1}^2(t) \exp(-2if_1 t) + E_{L_2}^2(t - \tau) \exp(-2i(f_1 + f_0)(t - \tau)) + \dots \right. \\ \left. \dots + E_{L_1}(t) E_{L_2}(t - \tau) \exp(-i(f_0 t - (f_1 + f_0)\tau)) + c.c. \right\} \quad (6)$$

Here, most of the components of the tunnelling current due to the linear polarization response come at very high frequencies, such as $2f_1$ and $2(f_1 + f_0)$, which is mixed with the tunnelling current signal at 0 Hz in the nanoantenna junction, thus cannot be measured by lock-in detection owing to the limited bandwidth of the high gain current amplifier. The cross-terms in the above equation, arising due to interference of the plasmon oscillations induced by the two frequency-shifted laser pulses in the nanoantenna junction contribute to the generation of the photocurrent,

which oscillates at the small offset frequency of $f_0 (< 1 \text{ kHz})$ in the nanoantenna junction,

$$I_1^T(t)|_{f_0} \propto \chi_1^2 |E_{L1}(t)E_{L2}(t-\tau)| \cos(f_0 t - (f_1 + f_0)\tau), \quad (7)$$

which can be measured in the experiments.

In the above analysis we have only considered the linear phase terms of the laser pulses, which is the group delay i.e. $f_1 t$ and $(f_1 + f_0)t$, where $f_1 = n f_r$. If we consider all the phase terms of the laser pulses, the electron tunnelling current can be expressed as: $I_1^T(t) \propto E_L(t) * E_L(t-\tau) \exp(i[\phi_1(t) - \phi_2(t-\tau)])$, where ϕ_1 and ϕ_2 are the complete temporal phases of the two laser pulses.

The phase terms for the two laser pulses can be expanded by Taylor's series with all linear and

nonlinear phase terms

$$\phi_1(t) = \phi_{0,CEP} + \phi_1'(t-t_0) + \frac{\phi_1''}{2!}(t-t_0)^2 + \frac{\phi_1'''}{3!}(t-t_0)^3 + \dots$$

and

$$\phi_2(t-\tau) = \phi_{0,CEP} + \phi_2'(t-\tau-t_0) + \frac{\phi_2''}{2!}(t-\tau-t_0)^2 + \frac{\phi_2'''}{3!}(t-\tau-t_0)^3 + \dots$$

The zero phase is the CEP of the laser pulse, $\phi_1'(t-t_0)$ and $\phi_2'(t-\tau-t_0)$ are the group delays of the laser pulses, $\phi_1'(t-t_0) = f_1(t-t_0)$ and $\phi_2'(t-\tau-t_0) = f_2(t-\tau-t_0)$. ϕ_1'' and ϕ_2'' the corresponding group delay dispersions (GDD), and so on. Hence,

$$I_1^T(t) \propto E_L(t) * E_L(t-\tau) \times \exp(i[\phi_1'(t-t_0) - \phi_2'(t-\tau-t_0)]) \times \exp(i[\phi_1''(t-t_0)^2 - \phi_2''(t-\tau-t_0)^2]) \times \exp(i[\phi_1'''(t-t_0)^3 - \phi_2'''(t-\tau-t_0)^3]) \quad (8)$$

The dispersion of the two laser pulses, i.e. GDD and higher order phases are identical in our experiment, $\phi_1'' \approx \phi_2'' \approx \phi''$, $\phi_1''' \approx \phi_2''' \approx \phi''' \dots$. Thus, the polarization term at a fixed delay of τ between the two pulses can be expressed as;

$$I_1^T(t)|_{\tau} \propto E_L(t) * E_L(t-\tau) \exp(-i[f_0 t - (f_1 + f_0)\tau]) \exp(-i[\phi'' \tau^2 - \phi''' \tau^3 + \dots]) \quad (9)$$

Therefore, measuring the linear polarization induced tunneling current arising due to one-

photon excitations in the nanoantenna junction as a function of the delay between the two pulses at their carrier offset frequency (f_0) enables complete temporal characterization of the laser pulses.

At $\tau = 0$ fs delay between the two pulses (pulse-1 and pulse-2), the above equation imitates the photo-assisted tunnelling current generated by the polarization response induced by a single laser pulse coming at the repetition rate of the small offset frequency of f_0 at the nanoantenna junction,

$$I_1^T(t)|_{f_0} \propto \chi_1^2 (E_{L1}(t)^2 + E_{L2}(t)^2 + 2|E_{L1}(t)E_{L2}(t)|\cos(f_0t)) \quad (10)$$

The electric field strengths of the pulse-1 and pulse-2 in our experiments are identical,

$E_{L1} \approx E_{L2} \approx \frac{E_0}{2}$, hence simplifying the above equation to;

$$I_1^T(t)|_{\tau=0} \propto \frac{1}{4} |\chi^{(1)} E_0(t)|^2 (1 + \cos(f_0t)) \quad (11)$$

In the case of a higher order nonlinear interaction of the laser pulses with the nanoantenna junction, the photo-assisted tunnelling current produced in the nanoantenna junction will be proportional to the multiple power of the corresponding terms in the total polarization response. For example, the photo-assisted tunnelling current due to a coherent two-photon absorption or the 2nd order nonlinear polarization response in the nanoantenna junction will be;

$$I_2^T(t) \propto \{\chi^{(2)} E_0(t)^2\}^2$$

$$I_2^T(t)|_{\tau=0} \propto \frac{1}{4} |\chi^{(2)} E_0(t)^2|^2 (1 + \cos(f_0t))^2 = \frac{1}{8} |\chi^{(2)} E_0(t)^2|^2 (3 + 4\cos(f_0t) + \cos(2f_0t)) \quad (12)$$

Similarly, the third order nonlinear response would generate a photo-assisted tunnelling current as given by;

$$I_3^T(t) \propto \{\chi^{(3)} E(t)^3\}^2$$

$$I_3^T(t)|_{\tau=0} \propto \frac{1}{8} |\chi^{(3)} E_0(t)^3|^2 (1 + \cos(f_0t))^3 = \frac{1}{8} |\chi^{(3)} E_0(t)^3|^2 (1 + \cos^3(f_0t) + 3\cos^2(f_0t) + 3\cos(f_0t))$$

$$I_3^T(t)|_{\tau=0} \propto \frac{1}{8} |\chi^{(3)} E_0(t)|^2 \left(1 + \frac{\cos(3f_0 t) + 3\cos(f_0 t)}{4} + 3 \frac{1 + \cos(2f_0 t)}{2} + 3\cos(f_0 t) \right) \quad (13)$$

Measurement of the time-resolved photo-assisted tunnelling current as a function of the delay between pulse-1 and pulse-2 at the lock-in frequency of $2f_0$ enables sampling of the 2nd order polarization response (or the 2nd order nonlinear electron oscillations) of the nanoantennas to

the ultrashort laser pulses; $I_2^T(t)|_{2f_0} = \frac{1}{8} |\chi^{(2)} E_{L1}(t) E_{L2}(t - \tau)|^2 \cos(2f_0 t - 2(f_1 + f_0)\tau)$. Likewise,

time-resolved measurement at $3f_0$ frequency in the lock-in detection enables sampling of the 3rd order nonlinear polarization response;

$I_3^T(t)|_{3f_0} = \frac{1}{8} |\chi^{(3)} E_1(t) E_2(t - \tau)|^3 \cos(3f_0 t - 3(f_1 + f_0)\tau)$. The oscillation period of the second

and third-order nonlinear electron oscillations will be one-half (~ 1.4 fs) and one-third (~ 0.9 fs) of the local plasmon oscillations (~ 2.7 fs), respectively. In the current experiments using laser power up to 220 pJ, the contributions of third-order nonlinear are usually weak.

In the intensity scaling experiment shown in Fig. 3e (main-text), measurement of photo-assisted tunnelling current at the lock-in frequency of f_0 at the zero delay between pulse-1 and pulse-2 would contain tunnelling currents arising mainly from the linear and second polarization responses, as can be understood from Eqn. (11)-(13).

$$I_1^T(t)|_{f_0} \propto \frac{1}{4} |\chi^{(1)} E_0(t)|^2 (\cos(f_0 t)) + \frac{1}{8} |\chi^{(2)} E_0(t)|^2 (4\cos(f_0 t)) \quad (14)$$

However, all the individual terms in the above equation arising due to different orders of the optical response follow completely different scaling laws with respect to the increasing field strengths of the incident laser pulses. Scaling of the photo-assisted tunnelling current in Fig. 3e for the lock-in frequency of f_0 shows a switching from the slope of one to the slope of two, indicating the presence of only linear response at the lower intensity of the laser pulses and presence of both linear as well as second order responses in the nanoantenna junction at higher intensity of the laser pulses. Third-order response, which would contribute to a slope of three in Fig. 3e are not present for the intensities of the laser pulses used in this experiment. The intensity of the laser pulses was intentionally kept below ~ 220 pJ in order to avoid irreversible

physical damage of the nanoantennas, which occurs at higher intensity of the laser pulses. Nevertheless, at a higher intensity (~ 300 pJ) of the laser pulses, third-order nonlinear response can be measured as shown in Fig. 3b (main text).

In the measurement shown in Fig. 3e (main-text), photo-assisted tunnelling current at the lock-in frequency of $2f_0$ can only arise due to the presence of the second-order response in the nanoantenna junction, as it shows a purely quadratic scaling in the experiment (Fig. 3e, main-text).

$$I_2^T(t)|_{\tau=0} \propto \frac{1}{8} |\chi^{(2)} E_0(t)|^2 (\cos(2f_0 t)) \quad (15)$$

Measurement of the amplitude of the photocurrent at the $2f_0$ frequency enables a direct access to the contribution of second-order nonlinear response in the photocurrent signal measured at the lock-in frequency of f_0 in Eqn. (12). At lower incident intensities of the laser pulse, i.e. below 100 pJ in Fig. 3e (main-text), only linear response can be excited in the junction of the nanoantennas, as the signal measured at the $2f_0$ frequency is below the noise level and the slope of the scaling curve is one. Only when the signal at $2f_0$ frequency start to emerge, i.e. above 100 pJ, the second order nonlinear response are generated in the nanojunction and this is when the slope of the scaling curve in the f_0 signal gradually changes its value from one to two. Therefore, by recording the homodyne beating signal at f_0 and its harmonic frequencies ($2f_0$ and higher), we demonstrate a direct identification of contributions of 1st and 2nd order light-induced polarizations (electron oscillations) induced in the nanoantenna junction in the measured photocurrents in the nanodevice.

Section IV. Comparison of the experimentally measured plasmon oscillations with the simulations

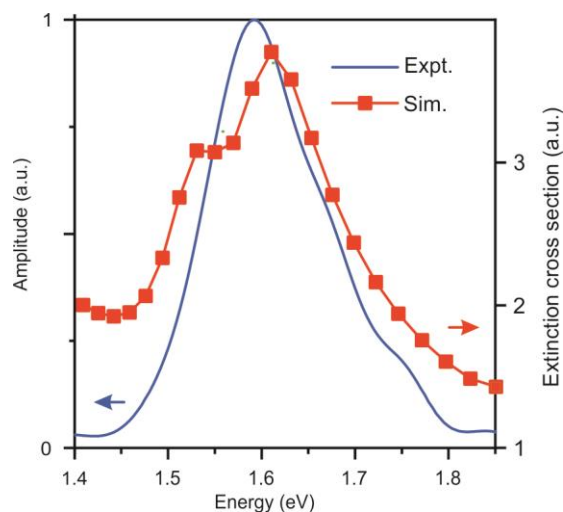


Fig. S3 | Comparison of the spectra of the experimentally measured and calculated plasmonic response of the nanoantenna junction. The blue curve shows the spectrum of the plasmonic response of the nanoantennas as measured in the experiments. The red curve shows the spectral shape of the plasmonic response as evaluated from the finite element simulations

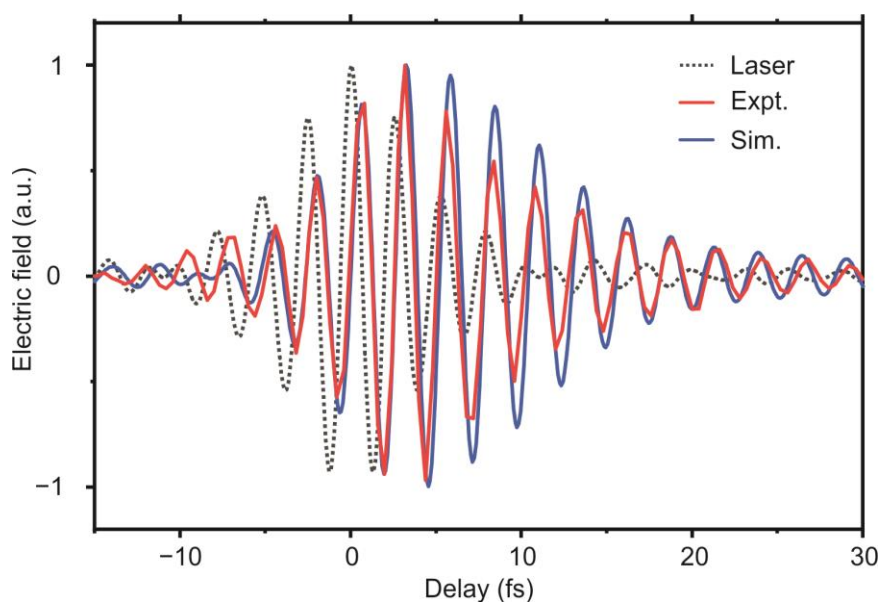


Fig. S4 | Comparison of the experimentally measured plasmon oscillations (the blue curve) with the electric field of the driving laser pulse (the dashed black curve) and the calculated plasmonic field (the red curve). The plasmon oscillations were measured by recording the variation of the laser-induced photocurrent as a function of the delay between pulse-1 and

pulse-2 laser pulses of slightly different carrier frequencies. Its delay is shifted by ~ 3 fs to the positive side to allow a direct comparison with the calculated plasmonic field.

Section V. Electron Transport across Nanoantenna Junction: Simmons Tunneling Model

Transport of electrons across the nanoantenna junction is primarily determined by the probability of electron tunneling between the apices of the two antennas (Fig. 4a), which in turn is significantly influenced by the occupation of high-lying electronic states above the Fermi level of Au nanoantennas ensuing absorption of photons from the laser pulse. We consider here a one-dimensional potential barrier model formed between the two apices of the nanoantennas and the vacuum tunneling gap as schematically shown in Fig. 4a of the main-text. In the perturbative regime of light-matter interaction, with Keldysh parameter² $\gamma > 1$, the photon-induced excitation of the electrons above the Fermi level can be modeled by an effective time-averaged Fermi population distribution function, f_{eff} . In the case of non-perturbative light-matter interaction, where $\gamma < 1$, the potential barrier formed between the apices of the nanoantennas can be significantly modified, this would happen at much higher local field strengths of the laser pulses at the nanoantenna junction, > 10 V/nm.

Briefly, by utilizing the Simmons tunneling model^{3,4}, the tunneling probability of electrons across the potential barrier (U_B) can be expressed as;

$$I(d, U_B) \propto \int_0^{\infty} f_{\text{eff}}(E) \times T(E, d, U_B) \times dE, \quad (16)$$

where d is the tunnelling gap between the apices of the nanoantennas, $T(E, d, U_B)$ is the tunneling probability of electrons, which is a function of the energy of the electron (E), tunneling gap (d) and the applied bias in the nanoantenna junction (U_B). $f_{\text{eff}}(E)$ can be modelled as a parameterized sum over different Fermi population distribution functions of amplitudes Δ_j , energy intervals E_j and energy widths δE_j :

$$f_{\text{eff}}(E) = \sum_{j=0}^N \frac{\Delta_j}{\left\{ \exp\left(\frac{E - (U_B + E_j)}{\delta E_j}\right) + 1 \right\}}. \quad (17)$$

The energy intervals of the excited electrons (E_j) and their widths (δE_j) can be simply considered as the multiples of the central photon energy of the laser pulse and its bandwidth;

$$E_j = j\hbar\omega.$$

References

- 1 Johnson, P. B. & Christy, R. W. Optical Constants of the Noble Metals. *Phys. Rev. B.* **6**, 4370 (1972).
- 2 Fedorov, M. V. L. V. Keldysh's "Ionization in the Field of a Strong Electromagnetic Wave" and modern physics of atomic interaction with a strong laser field. *J. Exp. Theor. Phys.* **122**, 449-455 (2016).
- 3 Simmons, J. G. Generalized formula for the electric tunnel effect between similar electrodes separated by a thin insulating film. *J. Appl. Phys.* **34**, 1793–1803 (1963).
- 4 Schroder, B. *et al.* Controlling photocurrent channels in scanning tunneling microscopy. *New J. Phys.* **22**, 033047 (2020).